JGR Solid Earth

RESEARCH ARTICLE
10.1029/2019JB018612

Evolution of Elastic and Mechanical Properties During Fault Shear: The Roles of Clay Content, Fabric Development, and Porosity

Abby R. Kenigsberg[1], **Jacques Rivière**[2], **Chris Marone**[1], **and Demian M. Saffer**[1]

[1]Department of Geosciences and Center for Geomechanics, Geofluids, and Geohazards, The Pennsylvania State University, University Park, PA, USA, [2]Department of Engineering Science and Mechanics, The Pennsylvania State University, University Park, PA, USA

Key Points:

- Due to grain size and enhanced fabric formation, smectite content within gouge acts as a primary control on evolution of elastic properties during shear
- Mechanical and elastic properties of smectite-rich gouges are controlled by fabric; those of smectite-poor gouge are controlled by porosity
- Shear fabric formation causes transient reduction in ultrasonic velocities and elastic moduli even as porosity decreases

Correspondence to:
A. R. Kenigsberg,
ark235@psu.edu

Citation:
Kenigsberg, A. R., Rivière, J., Marone, C., & Saffer, D. M. (2020). Evolution of elastic and mechanical properties during fault shear: The roles of clay content, fabric development, and porosity. *Journal of Geophysical Research: Solid Earth*, *125*, e2019JB018612. https://doi.org/10.1029/2019JB018612

Received 4 SEP 2019
Accepted 2 MAR 2020
Accepted article online 8 MAR 2020

Abstract Phyllosilicates weaken faults due to the formation of shear fabrics. Although the impacts of clay abundance and fabric on frictional strength, sliding stability, and porosity of faults are well studied, their influence on elastic properties is less known, though they are key factors for fault stiffness. We document the role that fabric and consolidation play in elastic properties and show that smectite content is the most important factor determining whether fabric or porosity controls the elastic response of faults. We conducted a suite of shear experiments on synthetic smectite-quartz fault gouges (10–100 wt% smectite) and sediment incoming to the Sumatra subduction zone. We monitored *Vp*, *Vs*, friction, porosity, shear and bulk moduli. We find that mechanical and elastic properties for gouges with abundant smectite are almost entirely controlled by fabric formation (decreasing mechanical and elastic properties with shear). Though fabrics control the elastic response of smectite-poor gouges over intermediate shear strains, porosity is the primary control throughout the majority of shearing. Elastic properties vary systematically with smectite content: High smectite gouges have values of *Vp* ~ 1,300–1,800 m/s, *Vs* ~ 900–1,100 m/s, *K* ~ 1–4 GPa, and *G* ~ 1–2 GPa, and low smectite gouges have values of *Vp* ~ 2,300–2,500 m/s, *Vs* ~ 1,200–1,300 m/s, *K* ~ 5–8 GPa, and *G* ~ 2.5–3 GPa. We find that, even in smectite-poor gouges, shear fabric also affects stiffness and elastic moduli, implying that while smectite abundance plays a clear role in controlling gouge properties, other fine-grained and platy clay minerals may produce similar behavior through their control on the development of fabrics and thin shear surfaces.

1. Introduction

Shear fabrics and clay alignment in fault gouges have been connected to both low overall frictional strength and reduction in friction with progressive shear (Carpenter et al., 2011; Faulkner et al., 2003; Haines et al., 2013; Ikari et al., 2009, 2015; Jefferies et al., 2006; Knuth et al., 2013; Logan & Rauenzahn, 1987; Niemeijer et al., 2010; Saffer & Marone, 2003; Sisbon, 1977; Wibberley & Shimamoto, 2003; Wojatschke et al., 2016). These factors, and the presence of the clay mineral smectite in particular, have been linked to low friction coefficient (μ = ~0.1) on major tectonic faults, including the San Andreas fault zone (Carpenter et al., 2011, 2012; Collettini et al., 2009; Jeppson & Tobin, 2015; Lockner et al., 2011) and shallow subduction plate boundaries (Carpenter et al., 2011, 2012; Deng & Underwood, 2001; Ikari et al., 2011; Ujiie et al., 2013; Wojatschke et al., 2016; Wu et al., 1975). Clay fabrics and clay nanocoatings formed during shear have also been identified as a weakening mechanism that can impact fault stability and the mode of failure (Collettini et al., 2009; Haines et al., 2009, 2013; Niemeijer et al., 2010; Schleicher et al., 2006; Wojatschke et al., 2016). For example, with increasing clay abundance, synthetic and remolded natural gouges exhibit an increasingly large peak in friction upon initial shear, followed by a rapid decrease in frictional strength. This peak and subsequent decay has been attributed to the formation and evolution of shear planes and fabrics (Haines et al., 2013; Ikari et al., 2009; Knuth et al., 2013; Logan & Rauenzahn, 1987; Saffer & Marone, 2003).

While many of the effects of shear fabrics and clays, and smectite clay in particular, are well studied (e.g., decrease in coefficient of friction and evolution of porosity), there are comparatively few studies of the combined effects of composition, shear fabric, and fault structure on the elastic properties of fault zones (Carpenter et al., 2014; Gettemy et al., 2004; Jeppson & Tobin, 2015; Kelly et al., 2017; Knuth et al., 2013).

Elastic waves have been used extensively to monitor changes in elastic properties during seismic cycles in both nature and laboratory settings (Brenguier et al., 2008; Scuderi et al., 2017), as well as to indirectly document changes in porosity, stress state, fault healing, crack sealing, and grain coordination during deformation in fault gouge and granular materials (Digby, 1981; Fortin et al., 2005; Kaproth & Marone, 2014; Khidas & Jia, 2012; Knuth et al., 2013; Mavko et al., 2009; Ryan et al., 2018; Schubnel et al., 2003; Shreedharan et al., 2019).

In general, porosity loss (i.e., compaction), stress changes, and fault damage are recognized as primary controls on seismic velocity evolution (*P* wave and *S* wave) during deformation and shearing (Audet et al., 2009; Dvorkin et al., 1999; Fortin et al., 2005, 2007; Hadley, 1976; Jia et al., 1999; Kaproth & Marone, 2014; Khidas & Jia, 2012; Knuth et al., 2013; Li et al., 1998, 2004; Li & Vidale, 2001; Mavko et al., 2009; Mavko & Nur, 1979; Nur et al., 1998; Popp & Kern, 1998; Unsworth & Bedrosian, 2004). However, recent work has revealed more complex variations in elastic properties than a simple monotonic stiffening due to progressive compaction, leading to the hypothesis that shear fabrics play an important role in governing wave speeds and elastic properties and may be closely linked to fault frictional strength (Haines et al., 2013; Jeppson & Tobin, 2015; Kelly et al., 2017; Knuth et al., 2013). For example, recent work has documented seismic anisotropy across the damage zone of the San Andreas fault due to the development of clay and clay fabrics, providing support for the argument that the fault may be mechanically weak and exhibit creep due to intrinsically weak fault materials (Jeppson & Tobin, 2015). A similar study focused on the Carboneras fault zone in southeast Spain found that the degree of seismic anisotropy in the fault zone varies as a function of fabric and foliation, indicating that these characteristics are important to consider when designing source-receiver geometries for seismic surveys and imaging of fault zones (Kelly et al., 2017).

In this study, we investigate the evolution of the mechanical and elastic properties of a range of synthetic smectite rich clay gouges as well as natural sediment from off the coast of Sumatra collected during International Ocean Discovery Program (IODP) Expedition 362 (precise sample locations can be found in McNeill et al., 2017). We conducted a series of direct shear experiments and report on the evolution of porosity, coefficient of friction, ultrasonic velocities, and elastic moduli during progressive shearing. Focusing on the role of gouge composition, we discuss (1) the links between the evolution of coefficient of friction and corresponding ultrasonic velocities; (2) the role fabrics play in controlling mechanical and elastic properties; and (3) proposed micromechanical processes controlling the evolution of mechanical and elastic properties throughout shear for a range of clay-rich gouges.

2. Materials and Methods

2.1. Shearing Experiments

We conducted double direct shear (DDS) experiments on synthetic smectite-quartz fault gouges ranging in composition from 10–100 wt% Ca-montmorillonite, as well as experiments on clay-rich sediments from IODP Expedition 362 off the coast of Sumatra. The quartz used for synthetic samples is Ottawa sand from U.S. Silica Company (99.9% SiO_2), and the Ca-montmorillonite is from St. Cloud Mining Company (~97% pure Ca-montmorillonite). As far as the natural samples are concerned, they sit atop the subducting Indian Plate and represent the "subduction input" materials in which the plate interface eventually forms. We tested two of these natural sediment samples; both contained ~20 wt% quartz, ~12–13 wt% plagioclase, ~2–3 wt% calcite, ~15 wt% kaolinite + chlorite, and ~50 wt% smectite + illite. One of the samples (362-U1480E-9H-1, 130–150 cm) contained a higher proportion of illite within the smectite-illite fraction (8 wt% smectite + 41 wt% illite), whereas the other (362-U1480F-74X-2, 79–93 cm) contained 19% smectite + 32% illite. The Sumatra samples have a more complicated composition that our synthetic faults (Table 1), including the presence of plagioclase feldspar, illite, chlorite, and kaolinite.

In our DDS configuration, two gouge layers are sandwiched between three grooved steel forcing blocks (Figure 1). The grooves ensure that shear occurs within the layers and not at the interface with the shear blocks (Anthony & Marone, 2005; Knuth & Marone, 2007; Saffer & Marone, 2003). The center forcing block is longer than the two side blocks to ensure that the nominal surface area remains constant throughout shear. Steel guide plates are secured to the sides of the sample to keep gouge from extruding. Using a leveling jig, each layer was constructed to a 5 mm initial layer thickness, except for experiments used for calibrations

Table 1
List of Experiments, Including Calibration Experiments (Bolded Experiment Numbers are Shown in the Figures and Include Porosity Values Based on Porosity Model [±2.5%])

Exp. #	Composition	Peak coefficient of friction	Initial thickness of single layer (mm)	Calculated grain density of multi-phase mixture (g/cm^3)	Initial porosity (%)	Final porosity (%)	Notes
p5212	100% smectite	0.42	8	2.1	N/A	N/A	Calibration of acoustic side blocks
p5213	100% smectite	0.33	8	2.1	N/A	N/A	Calibration of acoustic side blocks
p5214	100% smectite	0.35	3	2.1	N/A	N/A	Calibration of acoustic side blocks
p5215	100% smectite	0.38	3	2.1	N/A	N/A	Calibration of acoustic side blocks
p5216	**100% smectite**	**0.37**	**5**	**2.1**	**14.4**	**3.4**	**Periodic mass loss measured**
p5217	100% smectite	0.37	5	2.1	N/A	N/A	Periodic mass loss measured
p5145	90% smectite/10% quartz	0.37	3	2.155	N/A	N/A	Calibration of acoustic side blocks
p5148	90% smectite/10% quartz	0.33	8	2.155	N/A	N/A	Calibration of acoustic side blocks
p5149	**90% smectite/10% quartz**	**0.33**	**5**	**2.155**	**14.5**	**8.0**	**Periodic mass loss measured**
p5150	90% smectite/10% quartz	0.34	8	2.155	N/A	N/A	Calibration of acoustic side blocks
p5154	90% smectite/10% quartz	0.36	3	2.155	N/A	N/A	Calibration of acoustic side blocks
p5157	90% smectite/10% quartz	0.34	5	2.155	N/A	N/A	Periodic mass loss measured
p5039	70% smectite/30% quartz	0.43	3	2.265	N/A	N/A	Calibration of acoustic side blocks
p5040	70% smectite/30% quartz	0.41	3	2.265	N/A	N/A	Calibration of acoustic side blocks
p5043	70% smectite/30% quartz	0.37	8	2.265	N/A	N/A	Calibration of acoustic side blocks
p5052	70% smectite/30% quartz	0.41	5	2.265	N/A	N/A	Periodic mass loss measured
p5128	70% smectite/30% quartz	0.36	8	2.265	N/A	N/A	Calibration of acoustic side blocks
p5136	**70% smectite/30% quartz**	**0.37**	**5**	**2.265**	**17.8**	**12.1**	**Periodic mass loss measured**
p4808	50% smectite/50% quartz	0.49	5	2.375	N/A	N/A	Periodic mass loss measured
p4830	50% smectite/50% quartz	0.47	5	2.375	N/A	N/A	Periodic mass loss measured
p4853	50% smectite/50% quartz	N/A	23	2.375	N/A	N/A	No shear. Calibration of acoustic side blocks.
p4867	50% smectite/50% quartz	0.47	3	2.375	N/A	N/A	Calibration of acoustic side blocks.
p4912	**50% smectite/50% quartz**	**0.44**	**5**	**2.375**	**21.6**	**16.1**	**Periodic mass loss measured**
p4913	50% smectite/50% quartz	0.43	5	2.375	N/A	N/A	Periodic mass loss measured
p4947	50% smectite/50% quartz	0.41	8	2.375	N/A	N/A	Calibration of acoustic side blocks
p4962	50% smectite/50% quartz	0.41	8	2.375	N/A	N/A	Calibration of acoustic side blocks
p4977	50% smectite/50% quartz	0.44	7	2.375	N/A	N/A	Calibration of acoustic side blocks
p5129	30% smectite/70% quartz	0.46 (before rollover)	8	2.485	N/A	N/A	Calibration of acoustic side blocks

Table 1
(continued)

Exp. #	Composition	Peak coefficient of friction	Initial thickness of single layer (mm)	Calculated grain density of multi-phase mixture (g/cm^3)	Initial porosity (%)	Final porosity (%)	Notes
p5137	30% smectite/70% quartz	0.5 (before rollover)	5	2.485	N/A	N/A	Periodic mass loss measured
p5141	30% smectite/70% quartz	0.46 (before rollover)	8	2.485	N/A	N/A	Calibration of acoustic side blocks
p5142	30% smectite/70% quartz	0.5 (before rollover)	3	2.485	N/A	N/A	Calibration of acoustic side blocks
p5143	30% smectite/70% quartz	0.51 (before rollover)	3	2.485	N/A	N/A	Calibration of acoustic side blocks
p5144	**30% smectite/70% quartz**	**0.48 (before rollover)**	**5**	**2.485**	**27.0**	**18.8**	**Periodic mass loss measured**
p5167	10% smectite/90% quartz	0.54 (before rollover)	8	2.595	N/A	N/A	Calibration of acoustic side blocks
p5176	10% smectite/90% quartz	0.56 (before rollover)	5	2.595	N/A	N/A	Periodic mass loss measured
p5178	**10% smectite/90% quartz**	**0.57 (before rollover)**	**5**	**2.595**	**36.6**	**25.1**	**Periodic mass loss measured**
p5184	10% smectite/90% quartz	.054 (before rollover)	8	2.595	N/A	N/A	Calibration of acoustic side blocks
p5185	10% smectite/90% quartz	0.57 (before rollover)	3	2.595	N/A	N/A	Calibration of acoustic side blocks
p5189	10% smectite/90% quartz	0.55 (before rollover)	3	2.595	N/A	N/A	Calibration of acoustic side blocks
p5218	Sumatra input material (51% smectite + illite)	0.6 (before rollover)	5	2.586	N/A	N/A	Periodic mass loss measured
p5219	Sumatra input material (51% smectite + illite)	0.63 (before rollover)	3	2.586	N/A	N/A	Calibration of acoustic side blocks
p5223	Sumatra input material (51% smectite + illite)	0.57 (before rollover)	8	2.586	N/A	N/A	Calibration of acoustic side blocks
p5224	Sumatra input material (51% smectite + illite)	0.59 (before rollover)	3	2.586	N/A	N/A	Calibration of acoustic side blocks
p5225	**Sumatra input material (51% smectite + illite)**	**0.64 (before rollover)**	**5**	**2.586**	**33.0**	**25.5**	**Periodic mass loss measured**
p5226	Sumatra input material (51% smectite + illite)	0.58 (before rollover)	8	2.586	N/A	N/A	Calibration of acoustic side blocks
p5196	Sumatra input material (49% smectite + illite)	0.55 (before rollover)	5	2.652	N/A	N/A	Periodic mass loss measured
p5197	Sumatra input material (49% smectite + illite)	0.58 (before rollover)	3	2.652	N/A	N/A	Calibration of acoustic side blocks
p5199	Sumatra input material (49% smectite + illite)	0.57 (before rollover)	8	2.652	N/A	N/A	Calibration of acoustic side blocks
p5203	Sumatra input material (49% smectite + illite)	0.64 (before rollover)	3	2.652	N/A	N/A	Calibration of acoustic side blocks
p5204	**Sumatra input material (49% smectite + illite)**	**0.6 (before rollover)**	**5**	**2.652**	**41.1**	**31.0**	**Periodic mass loss measured**

which had initial thicknesses of 3, 5, 8, and 23 mm (Table 1; Kenigsberg et al., 2019). Tests were conducted at room temperature and humidity (12–73% relative humidity).

At the start of each test, we applied a layer normal stress of 25 MPa and allowed the samples to compact until reaching equilibrium (defined as stabilization of layer thickness) and then imposed shear by moving the center block at a velocity of 21.5 μm/s to total displacements of ~40–60 mm. Using load cells with a resolution of ±0.1 kPa (Kaproth & Marone, 2014), we measured shear and normal stress on the layers continuously throughout shear. We determine coefficient of friction by dividing shear stress by normal stress, assuming

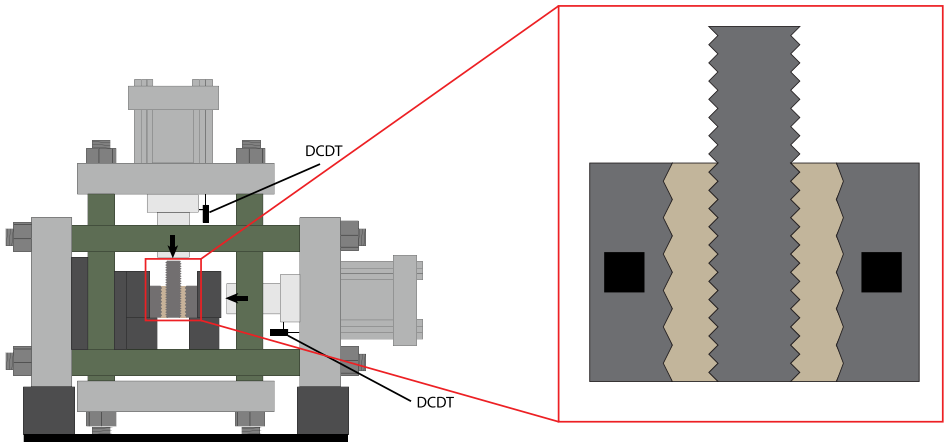

Figure 1. Left: Schematic of the biaxial shear apparatus and double direct shear sample. Right: Schematic of the double direct shear configuration with piezoelectric transducers within the side blocks (black rectangles).

zero cohesion (Figure 3). We also measured shear velocity and layer thickness with direct current displacement transducers (DCDTs) with a resolution of ± 0.1 μm.

Throughout experiments, we measured elastic wave speed using piezoelectric lead-zirconate-titanate transducers (PZTs, 500 kHz center frequency, 1.27 cm diameter) embedded in the side forcing blocks (Figures 1 and 2). We used a 15-bit data acquisition system and transmitted half-sine wave pulses through the DDS configuration every 10 ms throughout the experiment. One shear wave PZT acted as an ultrasonic transmitter, and the other acted as the receiver; *P* waves were generated via mode conversion. We recorded individual waveforms but use stacked waveforms during processing to improve signal-to-noise ratio.

2.2. Mass Loss and Porosity Calculations

Porosity evolution provides insight into micromechanical processes within the gouge layers and is important for determining elastic moduli from wave speed; hence, continuous monitoring of porosity during shear is a key element of our study (Figure 3). In the DDS configuration, material is lost from the actively shearing region both by entrainment along the steel forcing blocks and by geometric extrusion as the layer shears. We determine porosity using layer thickness measurements in tandem with a mass loss model. We briefly describe our approach to compute porosity as a function of shear strain here and refer the reader to Kaproth and Marone (2014) and Kenigsberg et al. (2019) for additional details.

As the layers are sheared, they thin due to both loss of gouge mass from the active shear zone (due to transport with the center block as it moves downward, so called "geometric thinning") and densification as the layers compact (Scott et al., 1994). While we are able to continuously monitor layer thickness, we must account for the material lost due to the geometric effect to correctly calculate the evolving mass of the actively shearing gouge material (Kaproth & Marone, 2014). With knowledge of the initial layer mass (measured directly at the time the layers are constructed), we define the bulk density and porosity of the layer throughout shear on the basis of conservation of mass. It is important to note that layer thickness measurements used in our porosity calculations do not account for material within the grooves of the forcing blocks. This material has a different density than the layer, and its evolution with strain differs from the layer (Kenigsberg et al., 2019).

We model this mass loss as a rectangular plug of material transported downward and out of the active shear zone with the center block. We first calculate an initial porosity based on known initial layer thickness, volume of sample, and mass of sample before shearing:

$$\rho_i = \frac{M_i}{(2hA) + V_T} \tag{1}$$

and

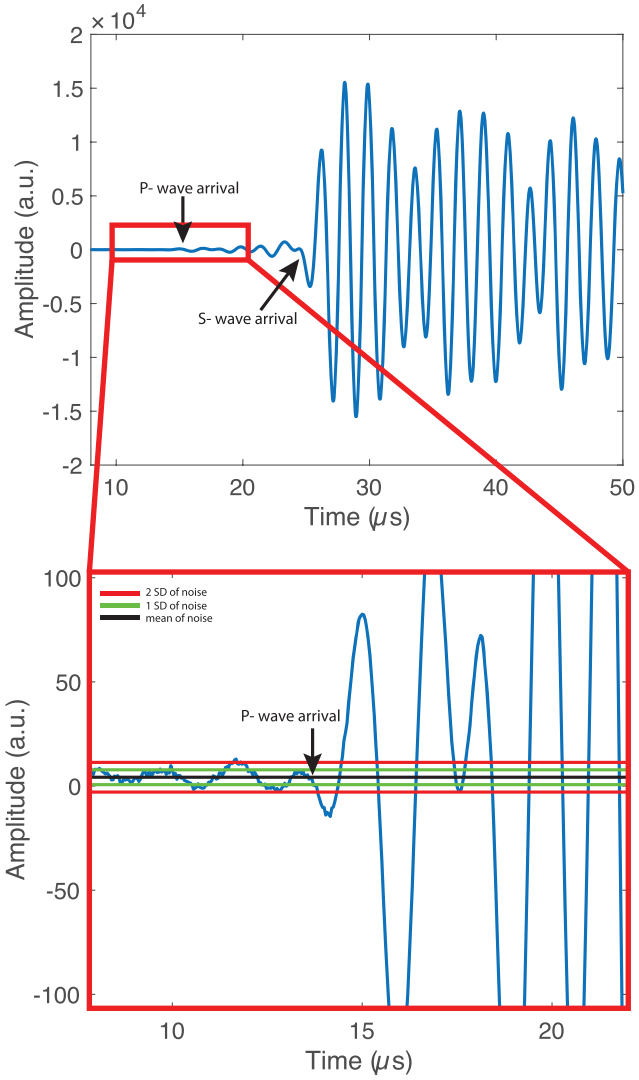

Figure 2. Example waveform in a.u., arbitrary units (p4830—50% smectite/50% quartz). *P* and *S* wave arrivals are picked at the zero crossing (black line) right before the signal has exceeded two standard deviation of the noise (red line).

$$\phi_i = \left(1 - \frac{\rho_i}{\rho_s}\right) \times 100, \tag{2}$$

where ρ_i is the initial layer bulk density, M_i is the initial mass, A is the nominal frictional contact area, h is single layer thickness, V_T is the total volume of the grooves in the forcing blocks, ϕ_i is the initial porosity (in percent), and ρ_s is the average solid grain density of the two-phase (or multiphase for Sumatra sediment) mixture (Table 1). For the case of a rectangular plug, the volume and mass lost through shear at any given time, n, are given by

$$M_{(n)} = M_i - M_L \tag{3a}$$

or

$$M_{(n)} = (\rho_{n-1} V_{n-1}) - (\rho_{n-1} V_L), \tag{3b}$$

where $M_{(n)}$ is the mass within the layer at time n, M_L is mass lost throughout shear, ρ_n is the density of the sample based on mass and volume, and V_L is volume lost throughout shear, given by

$$V_L = (2hWdy) + (2gv_T dy) \tag{4a}$$

and

$$V = (2hA) + V_T \ . \tag{4b}$$

V is the gouge volume that remains in the DDS configuration, dy is the distance sheared, g is the number of grooves/cm, W is the width of the blocks, v_T is the volume of a single tooth in the center block, and V_T is the volume of all of the grooves within the 10 cm × 10 cm shearing area.

Using the initial mass, density, and volume, we derive layer mass throughout shear from the known mass at a given time, M, and the calculated mass lost, M_L, due to sample extrusion. Bulk density and porosity are obtained from this mass, the measured volume of the layer (from layer thickness and known nominal contact area), and the average solid grain density (Kaproth & Marone, 2014; Kenigsberg et al., 2019). To verify the assumption of rectangular mass loss, we manually weighed the material that was extruded with the center block at multiple points during shearing and compared this to our modeled mass loss. The largest discrepancy between the predicted mass loss and the manually measured mass loss was 4 g, or ~3.5–4% of the total layer mass, and the porosity was measured within ±2.5%.

2.3. Ultrasonic Velocities and Elastic Moduli

Using *S* wave PZTs, we measured ultrasonic velocities by a time-of-flight technique, using first arrivals of *P* and *S* waves, layer thickness measurements, and an extensive set of empirical calibrations conducted to determine the wave travel time through the steel forcing block assembly (termed "zero time," Kenigsberg et al., 2019). To determine arrival times, we conducted manual picks at shear strains from 0–20 (Figure 2) and compared these with arrival times based on cross-correlation against a master waveform picked at zero shear strain. The time shift between the master waveform and every other waveform throughout the experiment is recorded and then added to our manually picked arrival time for the master waveform at zero shear strain. Based on our calibrations, we then subtract the zero time to obtain travel times of the *P* and *S* waves through the gouge layers themselves.

Using these velocities together with bulk densities defined by our mass loss model, we compute elastic moduli throughout shear (Digby, 1981; Kaproth & Marone, 2014; Knuth et al., 2013):

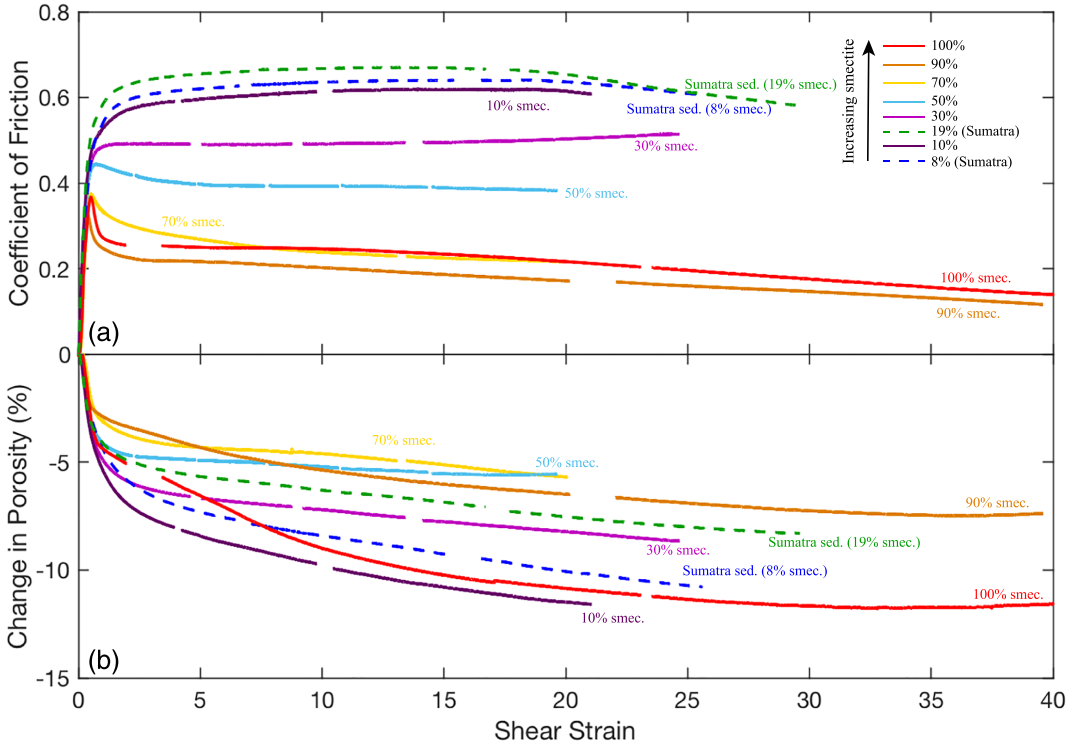

Figure 3. The coefficient of friction and change in porosity as a function of shear strain. The coefficient of friction decreases with increasing clay content in synthetic gouge mixtures. High smectite mixtures (50% and greater) exhibit a distinctive peak and subsequent decay due to fabric formation. Porosity decreases throughout the entire experiment for all mixtures. Porosity decreases most rapidly before peak friction and fabric formation and then reaches as steady state decrease as fabrics are formed. 100% and 90% smectite exhibit a more rapid decrease in porosity than other mixtures at intermediate shear strains (~0–8).

$$G = \rho V_s^2 \tag{5}$$

$$K = \rho V_p^2 - \frac{4}{3} G \tag{6}$$

where K is bulk modulus and G is shear modulus.

3. Results

3.1. Coefficient of Friction

Friction decreases systematically with clay abundance. Peak friction values are $\mu = 0.57$–0.63 for 10% smectite samples and Sumatra samples and decrease to $\mu = 0.33$ for 90–100% smectite samples (Figure 3a); residual friction values decrease from $\mu = 0.59$ for 10% smectite to 0.12 for 90–100% smectite gouge. This decrease is nonlinear—with high smectite gouges all exhibiting low residual friction ($\mu < 0.25$) and low smectite gouges all exhibiting high residual friction ($\mu > 0.5$); there is a rapid transition in friction between 30–70 wt% smectite. We note that the variations in friction are correlated with the abundance of smectite rather than total clay—as is evident from the behavior of the natural samples from Sumatra, which contain 8% and 19% smectite, but >50% clay, and exhibit friction similar to that for our synthetic mixtures with ≤30% smectite. We note minor exceptions to this trend wherein friction is slightly lower for our 90% smectite than our 100% smectite gouge, and we attribute this to the higher RH of the former experiment. Likewise, we note that for samples with lower smectite, there is a similar minor variation between some natural samples and the synthetics, which we attribute to the poly-mineralic composition of the natural sediments.

There is a similar difference in stress-strain evolution as a function of composition. Smectite-rich samples (≥50 wt%) exhibit a peak friction and subsequent decay at shear strains of ~1–2, whereas smectite-poor

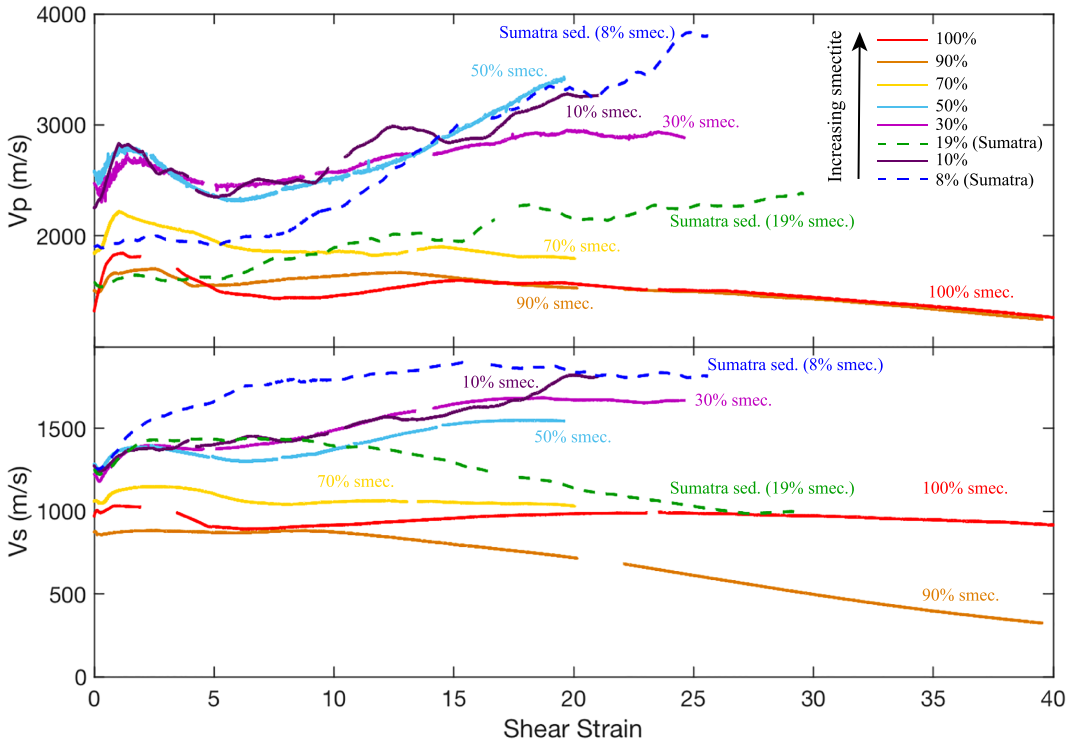

Figure 4. Absolute *P* and *S* wave velocities as a function of shear strain. In general, velocities decrease with increasing clay content. Decreases in velocities with increasing shear strain indicate that fabrics are controlling velocities as opposed to porosity loss. Due to the high portion of illite, the Sumatra sediments behave differently than the synthetic gouge mixtures.

samples exhibit a roll over in friction after initial loading and simply approach a steady-state value (Figure 3a) (Haines et al., 2013; Ikari et al., 2009; Knuth et al., 2013; Logan & Rauenzahn, 1987; Saffer & Marone, 2003). The natural samples—with high clay contents (~50% smectite + illite)—behave more similarly to the low clay synthetic gouges. This suggests that smectite may be the key factor in controlling frictional behavior, rather than total clay abundance.

3.2. Ultrasonic Velocities and Elastic Moduli

In general, the elastic responses of our samples fall into three main groups, which correspond to clay content: smectite-poor synthetic gouges (≤50 wt% smectite), smectite-rich synthetic gouges (>70 wt% smectite), and the Sumatra samples (~50 wt% smectite + illite; with <20 wt% smectite) (Figures 4, 5, and 6).

The smectite-poor synthetic gouge samples exhibit similar *Vp*, *Vs*, *K*, and *G* trends and values (Figures 4, 5, and 6). These gouges are characterized by similar initial (pre-shear) values of *Vp* (~2,300–2,500 m/s), *Vs* (~1,200–1,300 m/s), *K* (~5–8 GPa), and *G* (~2.5–3 GPa). Up to a shear strain of ~1.6, all exhibit increasing velocity and elastic moduli. This increase is followed by a relatively rapid decrease in *Vp* and *K*, while *Vs* and *G* stabilize. The 50% smectite sample is an exception to this trend and exhibits a decrease in *Vs* and *G* over these shear strains. Beyond shear strains of ~6, *Vp*, *Vs*, *G*, and *K* all increase throughout the rest of the experiments (at a shear strain of 20, *Vp* ~ 2,900–3,400 m/s, *Vs* ~ 1,500–1,800 m/s, *K* ~ 10–17 GPa, and *G* ~ 5–6 GPa) with the 50% smectite gouge having the largest values of *Vp* and *K* and 10% smectite having the largest values of *Vs* and *G* (Figure 6).

The smectite-rich synthetic gouges all exhibit similar trends in elastic moduli and velocities but span a larger range of values than the smectite-poor gouges (Figures 4 and 5). The 70% smectite sample exhibits higher velocities and larger elastic moduli than the 90% and 100% smectite gouges; however, in general, the smectite-rich samples (70–100 wt%) have much lower initial values of *Vp* (1,300–1,800 m/s, *Vs* (900–1,100 m/s), *K* (1–4 GPa), and *G* (1–2 GPa) than the quartz-rich (smectite-poor) gouges (Figure 6). The smectite-poor synthetic gouges, like their smectite-rich counterparts, exhibit an initial increase in *Vp*,

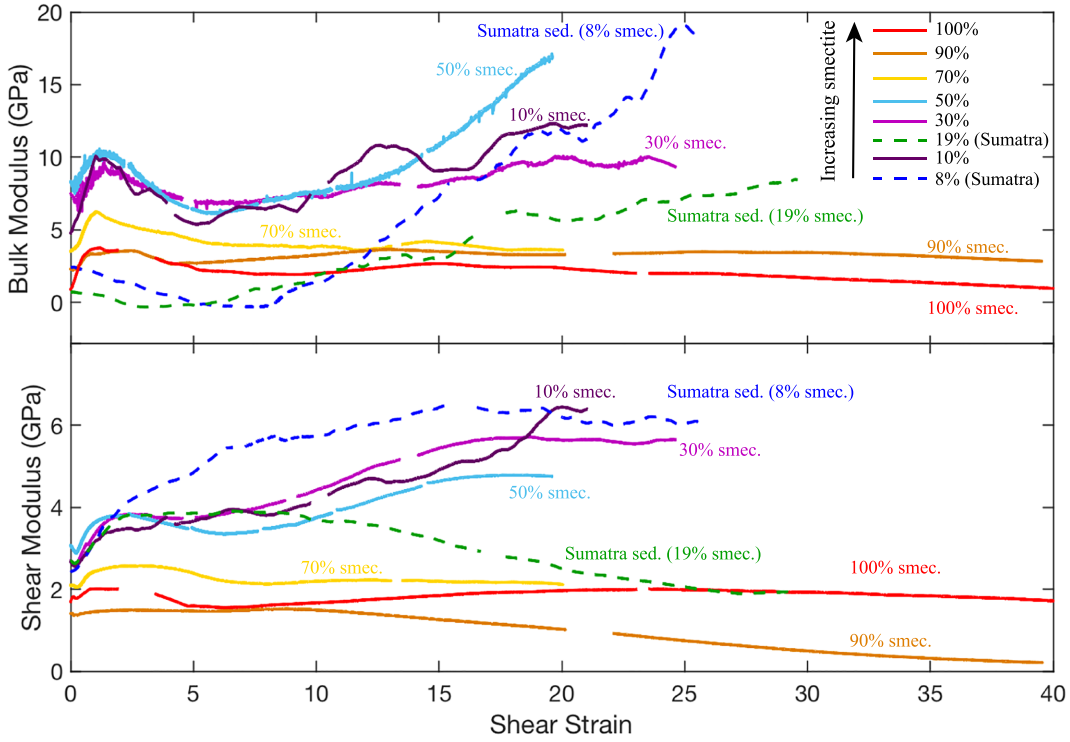

Figure 5. Shear and bulk moduli as a function of shear strain. High smectite synthetic gouge mixtures primarily exhibit decreasing elastic moduli as fabrics are weakening the gouges. Low smectite synthetic gouges have short periods of decrease due to optimally oriented fabrics but are primarily controlled by porosity loss and shear enhanced compaction as is shown by the increasing elastic moduli. The Sumatra sediments exhibit increases in elastic moduli except for the shear modulus of one of the samples indicating that fabrics may be pervasive as high shear strains for this sample.

Vs, *K*, and *G* and peak at a shear strain of ~1.6 (Figures 4 and 5). Unlike the smectite-poor samples, which exhibit increasing velocities and moduli beyond shear strains of ~6, the smectite-rich gouges exhibit decreasing velocities and moduli with continued shear (Figures 4 and 5). However, the 90% sample only displays an increase and peak in *Vp* and *K* while *Vs* and *G* remain stable (*Vp* ~ 1,700–2,200 m/s, *Vs* ~ 1,000–1,100 m/s, *K* ~ 4–6 GPa, *G* ~ 2–3 GPa). The 90% smectite sample—as is the case for frictional behavior—is a minor exception to this overall trend primarily for *Vs* and *G*, as it exhibits values that are lower than the 100% smectite case. Again, this is consistent with the higher relative humidity for the 90% smectite experiment as increased water content decreases the frictional strength of smectite (Ikari et al., 2007).

The Sumatra samples exhibit intermediate properties and more complex stress-strain behavior than the synthetic gouges. The two Sumatra samples exhibit initial values of *Vp* (~1,600–1,900 m/s) and *K* (~1–2 GPa) similar to the smectite-rich synthetic gouges (Figures 4 and 5); however, the pre-shear values of *Vs* (~1,200 m/s) and *G* (~2–3 GPa) are more similar to those of the smectite-poor synthetic gouges (Figures 4 and 5). The behavior of the Sumatra samples at higher shear strains is slightly more complex. As shear progresses, *Vp* and *K* for both Sumatra samples increase and follow the same general trend as our smectite-poor synthetic gouges, reaching maxima of *Vp* ~ 2,200–3,300 m/s and *K* ~ 6–12 GPa at a shear strain of 20. The two Sumatra samples have differing trends for *Vs* and *G*. The Sumatra sample with 8% smectite exhibits similar values and trends of *Vs* and *G* to the 10% smectite gouge (*Vs* ~ 1,800 m/s and *G* ~ 6 GPa at shear strain of 20). However, the Sumatra sample with 19% smectite exhibits similar *Vs* and *G* to the 10% smectite sample until a shear strain of ~8, after which it decreases to *Vs* and *G* values similar to the smectite-rich synthetic gouges (*Vs* ~ 1,100 m/s and *G* ~ 2 GPa at a shear strain of 20). Overall, the natural sample with 19 wt% smectite (51% smectite + illite) exhibits lower *Vp*, *Vs*, *K*, and *G* than the sample with 8 wt% (49% smectite + illite).

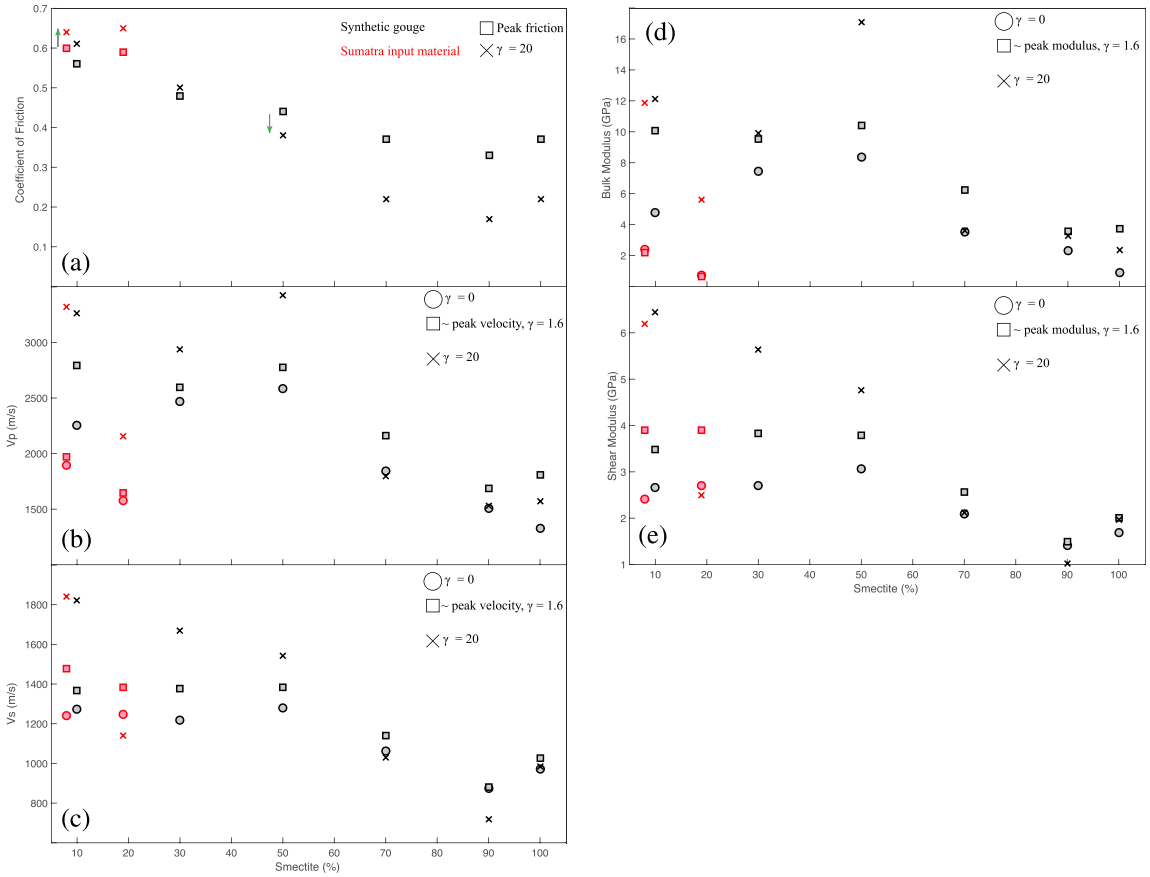

Figure 6. The coefficient of friction, *Vp*, *Vs*, and bulk (*K*) and shear (*G*) modulus as a function of smectite percentages at a shear strain of 0, local peak coefficient of friction (immediately after shear stress load up) and velocity/modulus, and at a shear strain of 20. Low smectite gouge mixtures exhibit an increase in the coefficient of friction (green arrow indicates increasing shear strain), *Vp*, *Vs*, *K*, and *G* as a function of shear strain whereas high smectite synthetic gouge mixtures exhibit a decrease in *Vp*, *Vs*, and the coefficient of friction (green arrow indicates increasing shear strain) as a function of shear strain due to fabrics weakening the gouge. *K* and *G* reach a peak and then decrease by a shear strain of 20. The Sumatra samples largely behave similarly to the low smectite synthetic gouge samples with the exception of *Vs* and *G* of the Sumatra sample with 19% smectite.

4. Discussion

Our experiments indicate that composition, shear fabric development, and porosity loss act in concert to control the mechanical and elastic properties of fault gouge. Importantly, we find that smectite content is a primary factor in determining whether shear fabric or compaction dominates the evolution of friction and elastic properties with shear. This is likely due to a combination of its intrinsic properties and hydration state and its fine grain size and grain morphology, which in turn strongly affect fabric development; for example, thin Riedel shears form in smectite-rich gouges due to its platy grain morphology and fine grain size (Haines et al., 2013). Shear fabrics reduce the coefficient of friction in smectite-rich synthetic gouges, resulting in a decay from peak friction and overall low residual friction (Collettini et al., 2009; Haines et al., 2009, 2013; Niemeijer et al., 2010; Schleicher et al., 2006; Wojatschke et al., 2016). As described in the following, we suggest that shear fabrics also provide an explanation for the evolution of elastic moduli and wave speeds, through a competition with porosity reduction.

4.1. Frictional Strength and Stress-Strain Behavior

In agreement with previous studies, we observe a peak and subsequent decay of the coefficient of friction in synthetic gouge samples with ≥50 wt% smectite (Figure 3) (Carpenter et al., 2011; Haines et al., 2009, 2013; Ikari et al., 2009, 2011; Logan et al., 1979; Niemeijer et al., 2010; Saffer & Marone, 2003; Wojatschke et al., 2016). With lower smectite abundance and increased quartz content, this peak diminishes and is eventually absent in synthetic gouge samples that have <50 wt% smectite. The characteristic peak and decay in

the coefficient of friction of smectite-rich gouges has been linked to shear fabric formation, particularly the rotation of shears that form as Riedel shears and then rotate to the Y-shear orientation with increasing shear strain and with aligned clay minerals that weaken the layer (Carpenter et al., 2011; Haines et al., 2013; Ikari et al., 2011; Niemeijer et al., 2010; Tembe et al., 2010; Wojatschke et al., 2016; Wu et al., 1975).

The Sumatra samples have a more complicated composition and, also, a more complicated explanation for the their frictional and stress-strain behavior. Though these samples both contain ~50 wt% smectite + illite (SI), these two samples are frictionally stronger than our 50% smectite synthetic gouge. The Sumatra samples contain a relatively small proportion of smectite (8 and 19 wt%; with the remaining SI composed of illite). This indicates that smectite, rather than total clay content, is probably the main control on strength and coefficient of friction. As suggested by Haines et al. (2013), this may be due to grain size, morphology, and the resulting thin Riedel shears formed in smectite (in comparison to illite that is slightly less platy and forms higher angle Riedel shears). Though illite is similar to smectite, it does not contain water interlayers and is non-swelling. Therefore, although still weak relative to framework silicates, it is frictionally stronger than smectite (under saturated conditions, μ = ~0.2–0.25 vs. μ = ~0.1 for smectite; Carpenter et al., 2011; Ikari et al., 2007; Kopf & Brown, 2003; Saffer & Marone, 2003). The Ca-montmorillonite smectite, on the other hand, is a swelling clay. The smectite structure is not charge-balanced and, therefore, attracts water into the structure causing smectite to be much weaker, especially at higher stresses (Casey et al., 2016; Saffer & Marone, 2003). However, in these natural samples, we observe a decrease in the coefficient of friction at high shear strains indicating that, with enough shear, it is possible for fabrics to form that in turn affect the strength, and possibly the elastic response, of these materials.

4.2. Porosity Reduction, Fabric Evolution, and Elastic Properties

Compaction (porosity loss) is commonly cited as the primary control on velocity changes during deformation of granular materials (e.g., Gettemy et al., 2004) and shear (Fortin et al., 2005, 2007; Hadley, 1976; Jia et al., 1999; Kaproth & Marone, 2014; Khidas & Jia, 2012; Knuth et al., 2013; Popp & Kern, 1998; Schubnel et al., 2003). As porosity decreases, velocity is expected to increase as pore space is lost and grain contact quality increases. However, in our experiments, there are many instances where *Vp* decreases even as porosity decreases (Figures 6 and 7). This implies that processes other than porosity reduction play a role in controlling wave speed and its evolution with shear.

In general, we observe that both velocity and elastic moduli vary with gouge composition and shear strain. At a given shear strain, increased smectite content leads to a reduction in *Vp*, *Vs*, *K*, and *G* (Figure 6). The roles of smectite content and shearing become more evident at higher shear strains, as *Vp*, *Vs*, *G*, and *K* all increase with strain in clay-poor gouges and decrease or remain steady in clay-rich gouges.

Figure 7 presents a compaction trend curve from an experiment (p5243) on 50% smectite 50% granular quartz that was compacted to ~60 MPa (with no shear). *Vp* should follow a similar trend in our experiments if porosity reduction was the sole mechanism operating in the gouge. We hypothesize that the significant departures from this compaction trend in our experiments, including changes opposite in sign to the trend, reflect fabric development, dominantly in the clay-rich gouges. In particular, the observations of decreasing *Vp* even as compaction occurs (Figure 7), as well as the decrease (or steady values) of *Vs*, *K*, and *G* with shearing, are all consistent with a model in which shear planes that form and then rotate parallel to the layer, develop, and mature. We posit that these features disrupt and slow wave propagation normal to the layers, which is consistent expectations for anisotropic media or thin, highly cracked materials (Budiansky & O'connell, 1976; Eshelby, 1957, 1961, 1963; Hudson, 1986; Jeppson & Tobin, 2015; Kelly et al., 2017; Mavko et al., 2009). Our observations show a correlation of the peak in ultrasonic velocity with the peak in friction (Figures 3 and 4), which supports the idea that throughgoing fabrics are a likely underlying cause. In addition to the decrease in *Vp* with decreasing porosity, there are also stages of rapid velocity increase with shear, exceeding the rate of velocity we see in the simple example of pure compaction (no shear). Rapid *Vp* increases occur at high shear strains in the smectite-rich synthetic gouges as well as the Sumatra samples, and we interpret this to reflect a component of shear enhanced compaction (Fortin et al., 2005, 2007; Khidas & Jia, 2012). Our findings are consistent with previous work documenting low seismic velocities within the damage zone of the San Andreas Fault associated with authigenic clay formation and clay fabric, interpreted as evidence that the fault zone is weak due to the presence of weak minerals (Carpenter et al., 2011, 2012; Jeppson & Tobin, 2015; Lockner et al., 2011).

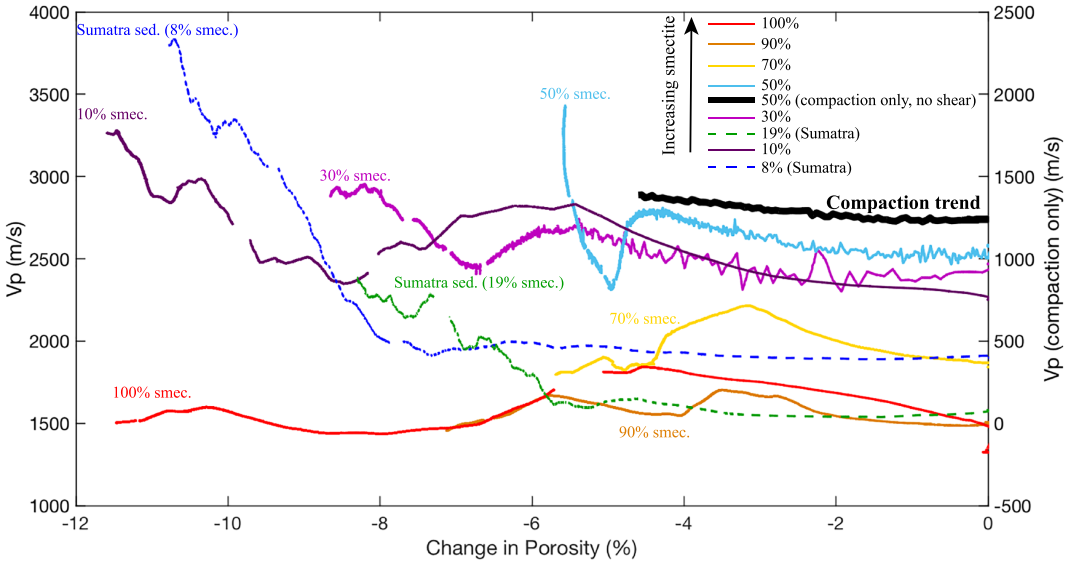

Figure 7. *P* wave velocity as a function of change in porosity. Shear strain is increasing as porosity is reducing. Changes in ultrasonic velocity throughout shear are generally attributed to porosity loss and compaction. The thick black line shows the compaction trend for an experiment (p5243) that was only compacted and was not sheared. However, we observe a deviation from this trend for our sheared experiments with decreases in velocity even as porosity decreases indicating that another processes in controlling velocity. We interpret decreases in velocity as porosity decreases as periods in which fabrics are controlling the velocity. High smectite synthetic gouges largely exhibit decreasing velocities as porosity decreases, indicating that fabrics are controlling these gouges for the majority of shear. Low smectite synthetic gouges exhibit short-term decreases in velocity. We attribute these decreases to periods in which fabrics are preferentially oriented perpendicular to the direction of wave propagation and, therefore, behave as barriers to the ultrasonic waves. The Sumatra sediments increase throughout shear indicating that they are largely controlled by porosity loss.

On the basis of our data, we suggest that fabric development affects the elastic properties and frictional evolution of the gouges differently, depending on the smectite content (Figure 6). For smectite-rich gouges, the development of shear planes and alignment of clay minerals leads to (1) the peak and subsequent decay in friction, as has been documented by detailed studies of microstructure and friction (e.g., Haines et al., 2009, 2013); (2) overall low frictional strength as pervasive Y-shears and Riedel shears are established; and (3) disruption and slowing of wave speeds across the layer and concomitant decreased elastic moduli with shearing.

In smectite-poor gouges, we suggest that wave speed and elastic moduli are controlled by a competition between fabric development and compaction. For gouges with <50 wt% smectite, and including the Sumatra samples, we do not observe a peak and decay in friction with strain (Figure 3), indicating that if shear fabrics or localized shear planes are developed, they do not exert significant control on the evolution of shear strength. However, the evolution of *Vp*, *Vs*, and elastic moduli is more complicated (Figures 4 and 5). Like the smectite-rich gouges, these materials exhibit a peak in wave speeds at shear strains of ~2 followed by a reduction in these quantities up to a shear strain of ~6, beyond which *Vp*, *Vs*, and elastic moduli all increase. As shear initiates, Riedel and P-shears form first and are not pervasive enough nor are they oriented in a way that they would interfere with wave propagation (Fortin et al., 2007; Haines et al., 2013; Kaproth & Marone, 2014; Khidas & Jia, 2012; Knuth et al., 2013). As shear progresses, Y-shears form, and Riedel shears begin to rotate subparallel to the direction of shear (often becoming Y-shears) and perpendicular to the direction of wave propagation (Haines et al., 2013; Logan et al., 1992; Logan & Rauenzahn, 1987). We posit that (1) the initial increase and peak in velocities and elastic moduli is related to increasing load and grain re-organization that leads to increased grain contacts and (2) the intermediate decrease in *Vp*, *Vs*, *G*, and *K* results from the formation of (perhaps poorly developed) Y-shears parallel to the direction of shear (as well as Riedel shears which are subparallel) and perpendicular to the direction of wave propagation (Haines et al., 2013; Kenigsberg et al., 2019; Logan et al., 1992; Logan & Rauenzahn, 1987). At higher shear strains, we suggest that shear enhanced compaction dominates and causes large increases in velocities and moduli.

The behavior of the Sumatra samples differs slightly from that of the smectite-poor synthetic gouges. These sediments are close to the threshold of ~50 wt% smectite that separates frictional and wave speed evolution with strain for our synthetic samples but, as noted above, contain <20 wt% smectite. Therefore, it is not surprising that the two Sumatra samples exhibit similar stress strain behavior to our 10 wt% smectite gouge, without a peak and decay in friction (cf. Figure 3). At high shear strains (~20–30), the coefficient of friction appears to decrease slightly. As these samples do contain ~50 wt% clays, this modest late-stage weakening could be due to fabric formation associated with the complex mineralogy of the material, intragranular cracking, or destruction of long force chains. Overall, the velocities and elastic moduli for both Sumatra samples, like those for smectite-poor synthetic gouges, appear to be controlled by porosity loss, as Vp and K increase at all shear strains. However, for the Sumatra sample with 51% SI (19% smectite), Vs and G decrease at high shear strains (~10–30), again perhaps indicating that fabrics may be forming in this sample at high strains—and that Vs and G are more sensitive to fabric formation than Vp and K.

It is important to note that previous studies have shown that it is not solely the composition of the gouge or anisotropic crystal structure of clay that leads to frictional weakness but also grain size and morphology that allows dramatic weakening (e.g., Haines et al., 2013); regardless of the dominant clay mineral (chlorite, illite, and smectite), similar shear fabrics are formed with shear. Further, Haines et al. (2013) show that, due to the fine grain size in clay-rich gouge, Riedel shears are >10 times thinner than those in coarser granular material (such as the quartz rich samples in this study) which allows deformation along these structures with minimal dilation or cataclasis. Therefore, our results may be relevant to clay-rich gouges having other compositions, but with similar grain sizes and distributions. This idea is consistent with previous work on purified smectite and illite gouges, which suggest similar frictional strengths for the two (Brown et al., 2003). However, the role of smectite abundance (rather than overall clay content) in leading to low frictional strength is evident from our data for natural samples from Sumatra, which show that their strength is controlled by smectite content rather than total clay (Figure 3). However, we cannot rule out the possibility that this apparent compositional effect is also, in part, related to the typical very fine grain size of smectite (e.g., Knuth et al., 2013). In addition, based on previous work from Haines et al. (2009), we can largely eliminate crystallographic preferred orientation as a primary control as Haines et al. (2009) found that with increased shear strain, there was minimal grain reorganization. While the crystallographic preferred orientation was much more intense for smectite than for other gouge material, it was still relatively weak (Haines et al., 2009).

4.3. Shear Planes and Clays in Natural Fault Gouges

Although our samples derived from natural material have much more complex compositions than two-component, synthetic clay-rich gouges, our data suggest that the coefficient of friction, elastic moduli, and wave speeds for these materials are all consistent with data for synthetic gouges with comparable smectite content. With some variations and complexities, as may be expected with natural samples, the properties of our Sumatra samples lie within the range observed for the synthetic smectite-poor gouges. The importance of smectite, rather than total clay abundance, is consistent with previous studies that have investigated the role of dehydration and clay transformation in the onset of mechanical changes on major faults (Hüpers et al., 2017; Lauer et al., 2017) and the role of smectite and associated fabrics in leading to fault weakening (Carpenter et al., 2011; Haines et al., 2013; Ikari et al., 2009, 2015).

5. Conclusions

We performed direct shearing experiments on a range of smectite-quartz synthetic gouges and natural sediments that form protolith for the Sumatra subduction thrust, in order to gain insight into the roles of composition, porosity, and fabric evolution in controlling fault physical properties. Although porosity reduction is commonly recognized as a dominant control on the elastic properties of sediments and other granular materials (e.g., Bachrach et al., 2000; Dvorkin et al., 1999; Kaproth & Marone, 2014; Knuth et al., 2013; Mavko et al., 2009; Mavko & Nur, 1979; Nur et al., 1998), we propose that, depending on smectite content, fabric and shear plane development also play a key role in the evolution of these properties with shearing. The frictional and elastic behavior of smectite-rich synthetic gouges is dominantly controlled by fabric development, particularly at high strains, whereas these properties in smectite-poor gouges evolve in response to the competing effects of fabric development and porosity loss, including shear-enhanced compaction.

Natural samples from Sumatra are controlled by similar micromechanical processes; in these materials, the low abundance of smectite and higher amounts of illite clays lead to behavior that mimics that of low smectite synthetic gouges but with possible indications that shear fabrics become increasingly important at high strains.

The interplay between gouge composition, fabric, and shear enhanced compaction elucidates the importance of these factors in governing the elastic and mechanical properties of faults.

In summary, we find that with increased smectite content, shear fabric formation controls elastic and mechanical properties causing the layer to destiffen, overpowering the effects of increased shear and decreased porosity. In contrast, low smectite content fault gouges are largely controlled by compaction, though these gouges are still affected by inferred fabric development. This hypothesized fabric formation which causes mechanical and frictional weakening also causes reduced elastic moduli indicating that fine-grained clay rich fault zones, such as smectite rich fault zones, may be expected to be both frictionally weak and compliant relative to fault zones formed in stronger minerals.

Acknowledgments
We thank S. Swavely for technical help in the laboratory and Parisa Shokouhi and Charles Ammon for key discussions. We also thank and acknowledge the work of Karissa Rosenberger, Michael Underwood, and Peter Vrolijk for their compositional analysis of the IODP samples used in this study. Finally, we thank two anonymous reviewers and associate editor Yves Bernabe, for the very extremely helpful reviews and suggestions. This research used samples provided by the International Ocean Discovery Program (IODP). Funding for this research was provided by the NSF U.S. Science Support Program (Post expedition award), GDL Foundation, DOE geothermal program (DOE EERE DE-EE0006762), and the NSF Geophysics program (NSF awards EAR-1215856, EAR-1520760, and EAR-1547286/1547441. All data available Penn State ScholarSphere (https://scholarsphere.psu.edu/).

References

Anthony, J. L., & Marone, C. (2005). Influence of particle characteristics on granular friction. *Journal of Geophysical Research*, *110*, B08409. https://doi.org/10.1029/2004JB003399

Audet, P., Bostock, M. G., Christensen, N. I., & Peacock, S. M. (2009). Seismic evidence for overpressured subducted oceanic crust and megathrust fault sealing. *Nature*, *457*(7225), 76–78. https://doi.org/10.1038/nature07650

Bachrach, R., Dvorkin, J., & Nur, A. M. (2000). Seismic velocities and Poisson's ratio of shallow unconsolidated sands. *Geophysics*, *65*, 559–564. https://doi.org/10.1190/1.1444751

Brenguier, F., Campillo, M., Hadziioannou, C., Shapiro, N. M., Nadeau, R. M., & Larose, E. (2008). Postseismic relaxation along the San Andreas fault at Parkfield from continuous seismological observations. *Science*, *321*(5895), 1478–1481. https://doi.org/10.1126/science.1160943

Brown, K. M., Kopf, A., Underwood, M. B., & Weinberger, J. L. (2003). Compositional and fluid pressure controls on the state of stress on the Nankai subduction thrust: A weak plate boundary. *Earth and Planetary Science Letters*, *214*, 589–603. https://doi.org/10.1016/S0012-821X(03)00388-1

Budiansky, B., & O'connell, R. J. (1976). Elastic moduli of a cracked solid. *International Journal of Solids and Structures*, *12*, 81–97. https://doi.org/10.1016/0020-7683(76)90044-5

Carpenter, B. M., Marone, C., & Saffer, D. M. (2011). Weakness of the San Andreas Fault revealed by samples from the active fault zone. *Nature Geoscience*, *4*, 251–254. https://doi.org/10.1038/ngeo1089

Carpenter, B. M., Saffer, D. M., & Marone, C. (2012). Frictional properties and sliding stability of the San Andreas fault from deep drill core. *Geology*, *40*, 759–762. https://doi.org/10.1130/G33007.1

Carpenter, B. M., Scuderi, M. M., Collettini, C., & Marone, C. (2014). Frictional heterogeneities on carbonate-bearing normal faults: Insights from the Monte Maggio fault, Italy. *Journal of Geophysical Research: Solid Earth*, *120*, 9062–9076. https://doi.org/10.1002/2014JB011176

Casey, B., Germaine, J. T., Flemings, P. B., & Fahy, B. P. (2016). In situ stress state and strength in mudrocks. *Journal of Geophysical Research: Solid Earth*, *121*, 5611–5623. https://doi.org/10.1002/2016JB012855

Collettini, C., Viti, C., & Marone, C. (2009). Fault zone fabric and fault weakness. *Nature*, *462*(7275), 907–910. https://doi.org/10.1038/nature08585

Deng, X., & Underwood, M. B. (2001). Abundance of smectite and the location of a plate-boundary fault, Barbados accretionary prism. *Bulletin of the Geological Society of America*, *113*, 495–507. https://doi.org/10.1130/0016-7606(2001)113<0495:AOSATL>2.0.CO;2

Digby, P. J. (1981). The effective elastic moduli of porous granular rocks. *Journal of Applied Mechanics*, *48*, 803–808. https://doi.org/10.1115/1.3157738

Dvorkin, J., Prasad, M., Sakai, A., & Lavoie, D. (1999). Elasticity of marine sediments: Rock physics modeling. *Journal of Geophysical Research*, *26*, 1781–1784.

Eshelby, J. D. (1957). The determination of the elastic field of an ellipsoidal inclusion, and related problems. *Proceedings of the Royal Society A: Mathematical, Physical and Engineering Sciences*, *241*, 376–396. https://doi.org/10.1098/rspa.1957.0133

Eshelby, J. D. (1961). Elastic inclusions and inhomogeneities. *Progress in solid mechanics*, *2*.

Eshelby, J. D. (1963). The distribution of dislocations in an elliptical glide zone. *Physica Status Solidi*, *3*, 2057–2060. https://doi.org/10.1046/j.1365-8711.2000.03496.x

Faulkner, D. R., Lewis, A. C., & Rutter, E. H. (2003). On the internal structure and mechanics of large strike-slip fault zones: Field observations of the Carboneras fault in southeastern Spain. *Tectonophysics*, *367*, 235–251. https://doi.org/10.1016/S0040-1951(03)00134-3

Fortin, J., Guéguen, Y., & Schubnel, A. (2007). Effects of pore collapse and grain crushing on ultrasonic velocities and *Vp*/*Vs*. *Journal of Geophysical Research*, *112*, B08207. https://doi.org/10.1029/2005JB004005

Fortin, J., Schubnel, A., & Guéguen, Y. (2005). Elastic wave velocities and permeability evolution during compaction of Bleurswiller sandstone. *International Journal of Rock Mechanics and Mining Sciences*, *42*, 873–889. https://doi.org/10.1016/j.ijrmms.2005.05.002

Gettemy, G. L., Tobin, H. J., Hole, J. A., & Sayed, A. Y. (2004). Multi-scale compressional wave velocity structure of the San Gregorio Fault zone. *Geophysical Research Letters*, *31*, L06601. https://doi.org/10.1029/2003GL018826

Hadley, K. (1976). Comparison of calculated and observed crack densities and seismic velocities in westerly granite. *Journal of Geophysical Research*, *81*.

Haines, S. H., Kaproth, B., Marone, C., Saffer, D., & van der Pluijm, B. (2013). Shear zones in clay-rich fault gouge: A laboratory study of fabric development and evolution. *Journal of Structural Geology*, *51*, 206–225. https://doi.org/10.1016/j.jsg.2013.01.002

Haines, S. H., van der Pluijm, B. A., Ikari, M. J., Saffer, D. M., & Marone, C. (2009). Clay fabric intensity in natural and artificial fault gouges: Implications for brittle fault zone processes and sedimentary basin clay fabric evolution. *Journal of Geophysical Research*, *114*, B05406. https://doi.org/10.1029/2008JB005866

Hudson, J. A. (1986). A higher-order approximation to the wave propagation constants for a cracked solid. *Geophysical Journal of the Royal Astronomical Society*, *87*, 265–274. http://ezaccess.libraries.psu.edu/login?url=http://search.ebscohost.com/login.aspx?direct=true&db=geh&AN=1987-021088&site=ehost-live&scope=site

Hüpers, A., Torres, M. E., Owari, S., McNeill, L. C., Dugan, B., Henstock, T. J., et al. (2017). Release of mineral-bound water prior to subduction tied to shallow seismogenic slip off Sumatra. *Science*, *356*, 841–844. https://doi.org/10.1126/science.aal3429

Ikari, M. J., Marone, C., & Saffer, D. M. (2011). On the relation between fault strength and frictional stability. *Geology*, *39*, 83–86. https://doi.org/10.1130/G31416.1

Ikari, M. J., Niemeijer, A. R., & Marone, C. (2015). Experimental investigation of incipient shear failure in foliated rock. *Journal of Structural Geology*, *77*, 82–91. https://doi.org/10.1016/j.jsg.2015.05.012

Ikari, M. J., Saffer, D. M., & Marone, C. (2007). Effect of hydration state on the frictional properties of montmorillonite-based fault gouge. *Journal of Geophysical Research*, *112*, B06423. https://doi.org/10.1029/2006JB004748

Ikari, M. J., Saffer, D. M., & Marone, C. (2009). Frictional and hydrologic properties of clay-rich fault gouge. *Journal of Geophysical Research*, *114*, B05409. https://doi.org/10.1029/2008JB006089

Jefferies, S. P., Holdsworth, R. E., Wibberley, C. A. J., Shimamoto, T., Spiers, C. J., Niemeijer, A. R., & Lloyd, G. E. (2006). The nature and importance of phyllonite development in crustal-scale fault cores: An example from the Median Tectonic Line, Japan. *Journal of Structural Geology*, *28*, 220–235. https://doi.org/10.1016/j.jsg.2005.10.008

Jeppson, T. N., & Tobin, H. J. (2015). San Andreas fault zone velocity structure at SAFOD at core, log, and seismic scales. *Journal of Geophysical Research: Solid Earth*, *120*, 4983–4997. https://doi.org/10.1002/2015JB012043

Jia, X., Caroli, C., & Velicky, B. (1999). Ultrasound propagation in externally stressed granular media. *Physical Review Letters*, *82*, 1863–1866. https://doi.org/10.1103/PhysRevLett.82.1863

Kaproth, B., & Marone, C. (2014). Evolution of elastic wave speed during shear-induced damage and healing within laboratory fault zones. *Journal of Geophysical Research: Solid Earth*, *119*, 4821–4840. https://doi.org/10.1002/2013JB010639

Kelly, C. M., Faulkner, D. R., & Rietbrock, A. (2017). Seismically invisible fault zones: Laboratory insights into imaging faults in anisotropic rocks. *Geophysical Research Letters*, *44*, 8205–8212. https://doi.org/10.1002/2017GL073726

Kenigsberg, A. R., Rivière, J., Marone, C., & Saffer, D. M. (2019). The effects of shear strain, fabric, and porosity evolution on elastic and mechanical properties of clay-rich fault gouge. *Journal of Geophysical Research: Solid Earth*, *124*, 10,968–10,982. https://doi.org/10.1029/2019JB017944

Khidas, Y., & Jia, X. (2012). Probing the shear-band formation in granular media with sound waves. *Physical Review E - Statistical, Nonlinear, and Soft Matter Physics*, *85*, 1–6. https://doi.org/10.1103/PhysRevE.85.051302

Knuth, M., & Marone, C. (2007). Friction of sheared granular layers: Role of particle dimensionality, surface roughness, and material properties. *Geochemistry, Geophysics, Geosystems*, *8*, Q03012. https://doi.org/10.1029/2006GC001327

Knuth, M. W., Tobin, H. J., & Marone, C. (2013). Evolution of ultrasonic velocity and dynamic elastic moduli with shear strain in granular layers. *Granular Matter*, *15*(5), 499–515. https://doi.org/10.1007/s10035-013-0420-1

Kopf, A., & Brown, K. M. (2003). Friction experiments on saturated sediments and their implications for the stress state of the Nankai and Barbados subduction thrusts. *Marine Geology*, *202*, 193–210. https://doi.org/10.1016/S0025-3227(03)00286-X

Lauer, R. M., Saffer, D. M., & Harris, R. N. (2017). Links between clay transformation and earthquakes along the Costa Rican subduction margin. *Geophysical Research Letters*, *44*, 7725–7732. https://doi.org/10.1002/2017GL073744

Li, Y., & Vidale, J. E. (2001). Healing of the shallow fault zone from 1994–1998 after the 1992 M7.5 Landers, California, earthquake. *Geophysical Research Letters*, *28*, 2999–3002.

Li, Y., Vidale, J. E., Aki, K., Xu, F., & Burdette, T. (1998). Evidence of shallow fault zone strengthening after the 1992 M 7. 5 Landers, California, earthquake. *Science*, *217–220*, 1996–1999.

Li, Y. G., Vidale, J. E., & Cochran, E. S. (2004). Low-velocity damaged structure of the San Andreas Fault at Parkfield from fault zone trapped waves. *Geophysical Research Letters*, *31*, L12S06. https://doi.org/10.1029/2003GL019044

Lockner, D. A., Morrow, C., Moore, D., & Hickman, S. (2011). Low strength of deep San Andreas fault gouge from SAFOD core: Nature. *472*, 82. https://doi.org/10.1038/nature09927

Logan, J., Dengo, C., Higgs, N., & Wang, Z.-Z. (1992). Fabrics of experimental fault zones: Their development and relationship to mechanical behavior. *Fault Mechanics and Transport Properties of Rocks*, *51*, 33–67.

Logan, J.M., Friedman, M., Higgs, N., Dengo, C., and Shimamoto, T., 1979, Experimental studies of simulated gouge and their application to studies of natural fault gouges: Analysis of Actual Fault Zones in Bedrock.

Logan, J. M., & Rauenzahn, K. A. (1987). Frictional dependence of gouge mixtures of quartz and montmorillonite on velocity, composition and fabric. *Tectonophysics*, *144*, 87–108. https://doi.org/10.1016/0040-1951(87)90010-2

Mavko, G., Mukerji, T., & Dvorkin, J. (2009). *The rock physics handbook: Tools for seismic analysis of porous media*. Cambridge, New York: Cambridge University Press.

Mavko, G., & Nur, A. (1979). Wave attenuation in partially saturated rocks. *Geophysics*, *44*, 161–178.

McNeill, L. C., Dugan, B., & Petronotis, K. E. (2017). Sumatra subduction zone: Proceedings of the International Ocean Discovery Program, 362: College Station, TX (International Ocean Discovery Program), v. 362.

Niemeijer, A., Marone, C., & Elsworth, D. (2010). Fabric induced weakness of tectonic faults. *Geophysical Research Letters*, *37*, L03304. https://doi.org/10.1029/2009GL041689

Nur, A., Mavko, G., Dvorkin, J., & Galmudi, D. (1998). Critical porosity: A key to relating physical properties to porosity in rocks. *The Leading Edge*, *17*, 357–362.

Popp, T., & Kern, H. (1998). Ultrasonic wave velocities, gas permeability and porosity in natural and granular rock salt. *Physics and Chemistry of the Earth*, *23*, 373–378. https://doi.org/10.1016/S0079-1946(98)00040-8

Ryan, K. L., Rivière, J., & Marone, C. (2018). The role of shear stress in fault healing and frictional aging. *Journal of Geophysical Research: Solid Earth*, *123*, 10,479–10,495. https://doi.org/10.1029/2018JB016296

Saffer, D. M., & Marone, C. (2003). Comparison of smectite- and illite-rich gouge frictional properties: Application to the updip limit of the seismogenic zone along subduction megathrusts. *Earth and Planetary Science Letters*, *215*, 219–235. https://doi.org/10.1016/S0012-821X(03)00424-2

Schleicher, A. M., Van Der Pluijm, B. A., Solum, J. G., & Warr, L. N. (2006). Origin and significance of clay-coated fractures in mudrock fragments of the SAFOD borehole (Parkfield, California). *Geophysical Research Letters*, *33*, L16313. https://doi.org/10.1029/2006GL026505

Schubnel, A., Nishizawa, O., Masuda, K., Lei, X., Xue, Z., & Guéguen, Y. (2003). Velocity measurements and crack density determination during wet triaxial experiments on Oshima and Toki granites. *Pure and Applied Geophysics*, *160*(5-6), 869–887. https://doi.org/10.1007/pl00012570

Scott, D. R., Marone, C. J., & Sammis, C. G. (1994). The apparent friction of granular fault gouge in sheared layers. *Journal of Geophysical Research*, *99*, 7231–7246.

Scuderi, M. M., Collettini, C., Viti, C., Tinti, E., & Marone, C. (2017). Evolution of shear fabric in granular fault gouge from stable sliding to stick slip and implications for fault slip mode. *Geology*, *45*, 731–734. https://doi.org/10.1130/G39033.1

Shreedharan, S., Rivière, J., Bhattacharya, P., & Marone, C. (2019). Frictional state evolution during normal stress perturbations probed with ultrasonic waves. *Journal of Geophysical Research: Solid Earth*, *124*, 5469–5491. https://doi.org/10.1029/2018JB016885

Sisbon, R. H. (1977). Fault rocks and fault mechanisms. *Journal of the Geological Society*, *133*, 191. https://doi.org/10.1144/gsjgs.133.3.0191

Tembe, S., Lockner, D. A., & Wong, T.-F. (2010). Effect of clay content and mineralogy on frictional sliding behavior of simulated gouges: Binary and ternary mixtures of quartz, illite, and montmorillonite. *Journal of Geophysical Research*, *115*, B03416. https://doi.org/10.1029/2009JB006383

Ujiie, K., Tanaka, H., Saito, T., Tsutsumi, A., Mori, J. J., Kameda, J., et al., & Expedition 343 and 343T Scientists (2013). Low coseismic shear stress on the Tohoku-Oki Megathrust determined from laboratory experiments. *Science*, *342*(6163), 1211–1214. https://doi.org/10.1126/science.1243485

Unsworth, M., & Bedrosian, P. A. (2004). Electrical resistivity structure at the SAFOD site from magnetotelluric exploration. *Geophysical Research Letters*, *133*, L12S05. https://doi.org/10.1029/2003GL019405

Wibberley, C. A. J., & Shimamoto, T. (2003). Internal structure and permeability of major strike-slip fault zones: The median tectonic line in Mie prefecture, Southwest Japan. *Journal of Structural Geology*, *25*, 59–78. https://doi.org/10.1016/S0191-8141(02)00014-7

Wojatschke, J., Scuderi, M. M., Warr, L. N., Carpenter, B. M., Saffer, D., & Marone, C. (2016). Experimental contraints on the relationship between clay abundance, clay fabric, and frictional behavior for the Central Deforming Zone of the San Andreas Fault. *Geochemistry Geophysics Geosystems*, *17*, 3865–3881. https://doi.org/10.1002/2016GC006406

Wu, F. T., Blatter, L., & Roberson, H. (1975). Clay gouges in the San Andreas fault system and their possible implications. *Pure and Applied Geophysics PAGEOPH*, *113*, 8795.